nature portfolio

https://doi.org/10.1038/s41565-021-01062-4

Supplementary information

Industrial scale production of fibre batteries by a solution-extrusion method

In the format provided by the authors and unedited

Supplementary Information for

Industrial scale production of fibre batteries by a solution-extrusion method

Meng Liao,[1†] Chuang Wang,[1†] Yang Hong,[1†] Yanfeng Zhang,[1] Xunliang Cheng,[1] Hao Sun,[1] Xinlin Huang,[1] Lei Ye,[1] Jingxia Wu,[1] Xiang Shi,[1] Xinyue Kang,[1] Xufeng Zhou,[1] Jiawei Wang,[1] Pengzhou Li,[1] Xuemei Sun,[1] Peining Chen,[1] Bingjie Wang,[1] Yonggang Wang,[2] Yongyao Xia,[2] Yanhua Cheng,[3] Huisheng Peng[1*]*

[1]State Key Laboratory of Molecular Engineering of Polymers, Department of Macromolecular Science and Laboratory of Advanced Materials, Fudan University, Shanghai 200438, China.

[2]Department of Chemistry and Shanghai Key Laboratory of Molecular Catalysis and Innovative Materials, Institute of New Energy, iChEM (Collaborative Innovation Center of Chemistry for Energy Materials) Fudan University, 200433 Shanghai, China.

[3]State Key Laboratory for Modification of Chemical Fibers and Polymer Materials, College of Materials Science and Engineering, Donghua University, Shanghai 201620, China.

[†]These authors contributed equally to this work.

**Correspondence and requests for materials should be addressed to Bingjie Wang (wangbingjie@fudan.edu.cn) and Huisheng Peng (penghs@fudan.edu.cn).*

This file includes:

Materials and Methods

1. Preparation of electrode inks and gel electrolyte for aqueous fibre Li-ion batteries (FLIBs)

Cathode inks for FLIBs were composed of active material, binders, and conductive agent in aqueous solution. The LA133 binder (60 g, 15 wt%, acrylonitrile co-polymer as the active ingredient) was first added to carbon nanotube (CNT) aqueous dispersion (600 g, 14 wt%, TNWPM-13-M8) to prepare the primary slurry for active material dispersion. The binder material of LA133 was selected due to its compatibility with various active materials as well as its capability to mediate the viscosity of mixtures. The obtained aqueous solution was then blended by a vacuum mixer (MSK-SFM-9-5L) for ~30 min to achieve a uniform dispersion. The cathode material, lithium manganese oxide (LMO, 75 g) was added to the above primary slurry, followed by a vigorous stirring process for ~1 h. Aqueous styrene butadiene rubber (SBR) emulsion was used as a secondary binder for the cathode ink to enhance the flexibility of the extruded fibres. Approximately 60 g aqueous SBR emulsion (50 wt%) was dissolved in the aqueous graphene dispersion (120 g, 15 wt%) and added to the cathode primary slurry to form a water-based mixture. This mixture was stirred for ~2 h before the final cathode ink was ready for extrusion. The mass ratio of cathode inks for FLIBs referred in **Fig. 2** and **Fig. 3** was 1 *(LA133)*:10 *(CNT aqueous dispersion)*:1.25 *(LMO)*:2 *(graphene dispersion)*:1 *(SBR)* without specific clarification.

Lithium titanium phosphate (LTP) was used as anode materials. The preparation procedure of anode inks was similar to that of cathode inks, *i.e.*, the active material of LTP was first dispersed in the uniform mixture of LA133/CNT aqueous dispersion and then blended with additional SBR binder in graphene dispersion. The mass ratio of anode inks for FLIBs referred in **Fig. 2** and **Fig. 3** was 1 *(LA133)*:10 *(CNT aqueous dispersion)*:1.5 *(LTP)*:2 *(graphene dispersion)*:1 *(SBR)* without specific clarification.

A mixture of chitosan and polyvinyl alcohol (PVA) and Li_2SO_4 were used to prepare gel electrolyte for extrusion. Chitosan (~120 g) that demonstrated good compatibility with Li_2SO_4 was first dissolved into acetic acid solution (3 L, 2 wt%) under vigorous stirring at room temperature for ~2 h. PVA solution (800 mL, 15 wt%) was further mixed with the above obtained chitosan solution to enhance mechanical properties of the polymeric framework. The lithium salt (Li_2SO_4) was added to the chitosan/PVA solution and blended at 80 ^oC for 1 h for extrusion.

2. Electrochemical measurements of fibre electrodes

Electrochemical activities of the extruded fibre electrodes were first evaluated before the continuous extrusion of full fibre batteries. Cathode (LMO) and anode (LTP) fibre electrodes were extruded by separated single channel (diameter of 0.6 mm) and then cut into 10 cm in length. Stainless-steel wires were used as lead wires in extruded fibre electrodes for test setup. Cyclic voltammograms and charge-discharge profiles of fibre electrodes (as working electrodes) were recorded in an electrolytic cell with active carbon as counter electrode and Ag/AgCl as reference electrode measured by CHI 660E electrochemical workstation.

3. Modulations of rheological properties

The apparent viscosity as a function of shear rate for cathode and anode inks was shown in **Supplementary Fig. 1**. Both cathode and anode inks constituted of LA133/SBR as the binder and CNT/graphene as the conductive additive. In cathode inks, the mass ratios of LMO: CNT: SBR: graphene: LA133 were 8.3: 9.3: 3.3: 2: 1 with a total solid material concentration of ~309 mg/mL. In anode ink, the mass ratios of LTP: CNT: SBR: graphene: LA133 were 10: 9.3: 3.3: 2: 1 with a total solid material concentration of ~330 mg/mL. The apparent viscosities of the above two inks decreased with the decreasing shear rate, exhibiting typical shear-thinning and non-Newtonian behavior. The high concentration of solid materials resulted in high zero shear viscosity approaching 20 Pa·s for both LMO and LTP electrode inks. The storage modulus (G′) and loss modulus (G″) of the LMO and LTP electrode inks as a function of shear stress were shown in **Supplementary Fig. 1c**. Generally, storage modulus described the solid response of the inks at low shear stress conditions, and the loss modulus reflected the liquid response of the inks at high shear stress conditions. The storage modulus plateaus approached 1 kPa under low shear stress for our electrode inks, which was higher than the relevant loss modulus. In this region, electrode inks would perform a solid response owing to elastic modulus in domination, which was crucial for coagulation. Both electrode inks demonstrated a relatively high yield stress of around 100 Pa, corresponding to the intersection of the elastic modulus and viscous modulus. Beyond the yield point, G″ surpassed G′ upon increasing shear stress. In this region, electrode inks exhibited viscous deformation with good fluidity, ensuring the stable fluxion in the narrow channels of spinneret. The high elastic modulus and yield stresses were essential to efficient solution-extrusion and coagulation processes of fibre electrodes. Last but not least, both LMO and LTP inks demonstrated nearly unchanged G′ and G″ upon the time elongation, further illustrating their stable rheological properties under shearing.

4. Finite element simulation of electrode ink in tapered spinneret

The fluid flow was simulated by solving the incompressible Navier-Stokes equations.

The dynamics of fluid was defined by Navier-Stokes equations:

$$\rho(\mathbf{u}\cdot\nabla)\mathbf{u} = \nabla\cdot(-\mathrm{p}\mathbf{I} + \mu(\nabla\mathbf{u} + (\nabla\mathbf{u})^{\mathrm{T}}))$$

$$\nabla\cdot\mathbf{u} = 0$$

where ρ is density, u is velocity, p is pressure, μ is the viscosity of electrode ink and I is identity matrix. The solid surface was applied for non-slipping conditions. We used two-dimensional axial symmetry geometry. The boundary condition was 5 mm/s velocity on the inlet boundary and zero pressure on the outlet boundary. The viscosity of the fluid was 10 Pa·s and the density was 1300 kg/m^3. The viscous stress was calculated by mu*(d*w*/d*r*+d*u*/dz) and the magnitude of velocity was calculated by sqrt(u^2+w^2), where *mu* was the viscosity of the fluid, *w* and *u* were the vertical and radial component of the velocity(*u*), respectively. And *z* and *r* represented the space coordinates of vertical and radial direction, respectively.

5. Scaled-up production of fibre batteries (FLIBs)

Continuous production of extruded fibre batteries involves a sequence of 1) slurry mixing, 2) extrusion, 3) coagulation, 4) drying and 5) collection steps. Specifically, in the slurry mixing step, as-prepared electrode inks and the gel electrolyte, which were stored in three separate storage tanks, were thoroughly mixed (stirring rate: 200 r/min). After mixing, the electrode inks were extruded through the two inner channels in the spinneret by booster pumps (revolving speed: 1-14 r/min; pressure: 0.1-1 MPa; volumetric flux: 4-60 mL/min). Gel electrolyte was extruded through the outer channel of the spinneret by a booster pump (revolving speed: 5-70 r/min; pressure: 0.1-1 MPa; volumetric flux: 20-300 mL/min). The extruded FLIBs were collected in an aqueous coagulation bath containing 1.75 M NaOH and 2 M Li_2SO_4 before they were drawn. Hydroxide ions in the coagulation bath penetrate the gel electrolyte layer of the extruded FLIBs and neutralize the residual acetic acid inside the gel electrolyte. As acetic acid is removed, the basic environment induces the precipitation of chitosan, forming a compact polymer network in the gel electrolyte. This solidified network effectively stabilizes the gel electrolyte around the two fibre electrodes and separates them. The as-prepared batteries were subsequently washed with 2 M Li_2SO_4 solution in another bath to remove residual NaOH before they were dried and collected on a winding spool. The average temperature of the drying oven was maintained at 50 ^{o}C and the draw ratio for the fibre batteries was 1:3. The collected fibre batteries were then encapsulated with flexible PTFE tubes to prevent the evaporation of water from the gel electrolyte (**Supplementary Fig. 5**).

6. Characterizations of FLIBs

Extruded FLIBs were cut into 10 cm long samples. Stainless-steel lead wires were connected with each parallel fibre electrode inside the fibre batteries and flexible PTFE tubes were used as encapsulations. Galvanostatic charge-discharge profiles were recorded on a battery testing system (LAND CT2001A). Applied current density and specific capacity were calculated based on the loading mass of active materials (*e.g.*, LMO and LTP) in FLIBs. The FLIB delivered energy density of 21.9 Wh/kg or 24.3 Wh/L calculated from the weight or volume of both cathode and anode fibres, which is comparable to previous reports.[1-3] Electrochemical impedance spectroscopy (EIS) measurement was conducted on the CHI 660E electrochemical workstation with an AC voltage of 5 mV amplitude at the frequency range of 10^5 to 0.1 Hz. Bending tests of the fibre battery were conducted on a set of home-made stepper motors (**Supplementary Fig. 15**). The fibre battery was bent at a frequency of 2.5 Hz.

7. Preparation of electrode inks and gel electrolyte for aqueous fibre Zn-MnO_2 batteries (FZMBs)

Active materials of MnO_2 and Zn powder were utilized for the preparation of cathode and anode inks, respectively. For cathode inks, MnO_2 was first dispersed into the uniform mixture of LA133/CNT aqueous dispersion and then blended with additional SBR binder in graphene dispersion. Mass ratios of cathode inks for aqueous FZMBs referred in **Fig. 2** were 1 (*LA133*):10 (*CNT aqueous dispersion*):1 (*MnO_2*):2 (*graphene dispersion*):1 (*SBR*) without specific clarification. As for anode inks, the mass ratios were 1 *(LA133)*:10 *(CNT aqueous dispersion)*:2 *(Zn powder)*:2 *(graphene dispersion)*:1 *(SBR)*. The zinc salt of $ZnSO_4$ was dissolved into the chitosan/PVA solution to obtain the 1 M $ZnSO_4$ aqueous gel electrolyte in the coagulation bath.

8. Preparation of electrode inks and gel electrolyte for aqueous fibre Na-ion batteries (FSIBs)

$Na_{0.44}MnO_2$ and $NaTi_2(PO_4)_3$ were utilized as active materials of cathode and anode, respectively. For cathode inks, the active material of $Na_{0.44}MnO_2$ was first dispersed into the uniform mixture of LA133/CNT aqueous dispersion and then blended with additional SBR binder in graphene dispersion. The mass ratios of cathode inks for aqueous FSIBs referred in **Fig. 2** were 1 *(LA133)*:10 *(CNT aqueous dispersion)*:1 *($Na_{0.44}MnO_2$)*:2 *(graphene dispersion)*:1 *(SBR)* without specific clarification. As for anode inks, the mass ratios were 1 *(LA133)*:10 *(CNT aqueous dispersion)*:1.8 *($NaTi_2(PO_4)_3$)*:2 *(graphene dispersion)*:1 *(SBR)*. The sodium salt of Na_2SO_4 was dissolved into the chitosan/PVA solution to obtain the 1 M Na_2SO_4 aqueous gel electrolyte in the coagulation bath.

9. Fabrication and characterization of FLIB textile

The weaving operation of the textile battery was made on a rapier loom (Tong Yuan Textile Machinery Co., Ltd.). The weaving diagram was presented in **Fig. 3a**. FLIBs were woven as weft and common fibre materials as warp to obtain large area textile batteries. To estimate the durability of the textile battery upon typical home launderings, an accelerated washing process was performed in a standard washing machine following international standards issued in the European Union (IEC 61233-2), USA (UL 2054), and China (GB 31241). Each wash cycle contained 5 textile battery samples and additional steel balls, which were added to simulate the mechanical effects of washing (**Supplementary Fig. 20**). The capacity of the textile battery was measured after every 20 washing cycles.

10. Fabrication of energy harvesting textiles

Ti wire (diameter of 127 μm, Alfa Aesar) was used as the substrate of photoanode. First, the Ti wire was sequentially cleaned by sonication in deionized water, acetone and isopropanol for 5 min each. Then TiO_2 nanotubes were grown on Ti wire by an anodic oxidation in a water bath. A 0.3 wt% NH_4F/ethylene glycol (Sinopharm) solution containing 8 wt% H_2O was prepared as the electrolyte. The growth was operated in a two-electrode system with Ti wire as anode and Pt plate as cathode at 60 V for 2 h at 40 °C. The modified Ti wire was first washed by deionized water and then annealed at 500 °C for 60 min. After cooled to 110 °C in the furnace, the wire was immersed in Z907 (Shanghai MaterWin New Materials Co., Ltd.) solution (0.3 mM, mixture solvent of dehydrated acetonitrile (Adamas) and tert-butanol (Sinopharm) with an equal volume ratio) for 16 h. Next, CuI was drop-coated onto the modified Ti wire in a glovebox at 110 °C. CuI solution was prepared by dissolving 0.16 M cuprous iodide (Aladdin), 1-methyl-3-ethylimidazolium thiocyanate (Lanzhou Greenchem ILs) and 0.2 mM 4-tert-butylpyridine (Adamas) in acetonitrile.

Silver-plated nylon yarns were woven in the warp direction as the counter electrodes for energy harvesting textile. The cotton threads and modified photoanode fibres were then alternately woven in the weft direction[4,5]. Current density-voltage curves of the energy harvesting part were recorded by a Keithley 2400 Source Meter under the illumination (100 mW/cm^2) of simulated AM1.5 solar light from a solar simulator (Oriel-Sol3A 94023A equipped with a 450 W Xe lamp and an AM1.5 filter). Electrochemical measurements were performed on an electrochemical workstation (CHI 660E).

11. Fabrication of displaying textiles

Commercial ZnS phosphors (Shanghai Keyan Phosphor Technology Co., Ltd.) were dispersed into fluoro-rubber solution (10 wt%, N-methyl pyrrolidone as solvents) with a weight ratio of 2.5:1 by blending for 6 h at 70 ℃. Stainless steel yarns (diameter of 200 μm, Jiangsu Huafei Alloy Material Technology Co., Ltd.) were dip-coated by above ZnS phosphor dispersions, passed through (8 m/min) a scraper ring with the inner diameter of 0.5 mm, and then dried at temperature of 120 ℃. The ZnS-coated yarns were twisted with conductive copper yarns (diameter of 100 μm) through a rotating motor at the rotating speed of 300 r/min and then dip-coated by polyvinylidene fluoride (PVDF) solutions (15 wt%, N-methyl pyrrolidone as solvents) for electrical insulation. Electroluminescent fibres were dried at temperature of 120 ℃ before use. Silver-plated nylon yarns were woven in the warp direction as the electrical connections for displaying textile. The cotton threads and electroluminescent fibres were then alternately woven in the weft direction.

12. Characterizations

Micro-morphologies of fibre electrodes were characterized by scanning electron microscopy (SEM, Zeiss FE-SEM Ultra 55 operated at 5 kV). Electrochemical performances were obtained from a battery testing system (LAND CT2001A) and electrochemical workstation (CHI 660E). Mechanical properties of fibre batteries were characterized by materials testing machine (Hengyi T0086). The bending stiffness was characterized by a dynamic mechanical analyzer (Q800, TA Instruments). The samples of ~4 cm in length and ~700 μm in diameter were tested with a frequency sweep (0.1-10 Hz) under controlled displacement (50 μm) at 25 °C. Photographs were taken by a digital camera (SONY A6000, Japan). Rheological properties were characterized by rotational rheometer (Thermofisher HAAKE MARS III). Bending tests of the fibre battery were conducted on a set of home-made stepper motors (**Supplementary Fig. 15**). The fibre battery was bent to a bending radius of ~1 cm using a load of 0.1 N and speed of 0.4 s per cycle.

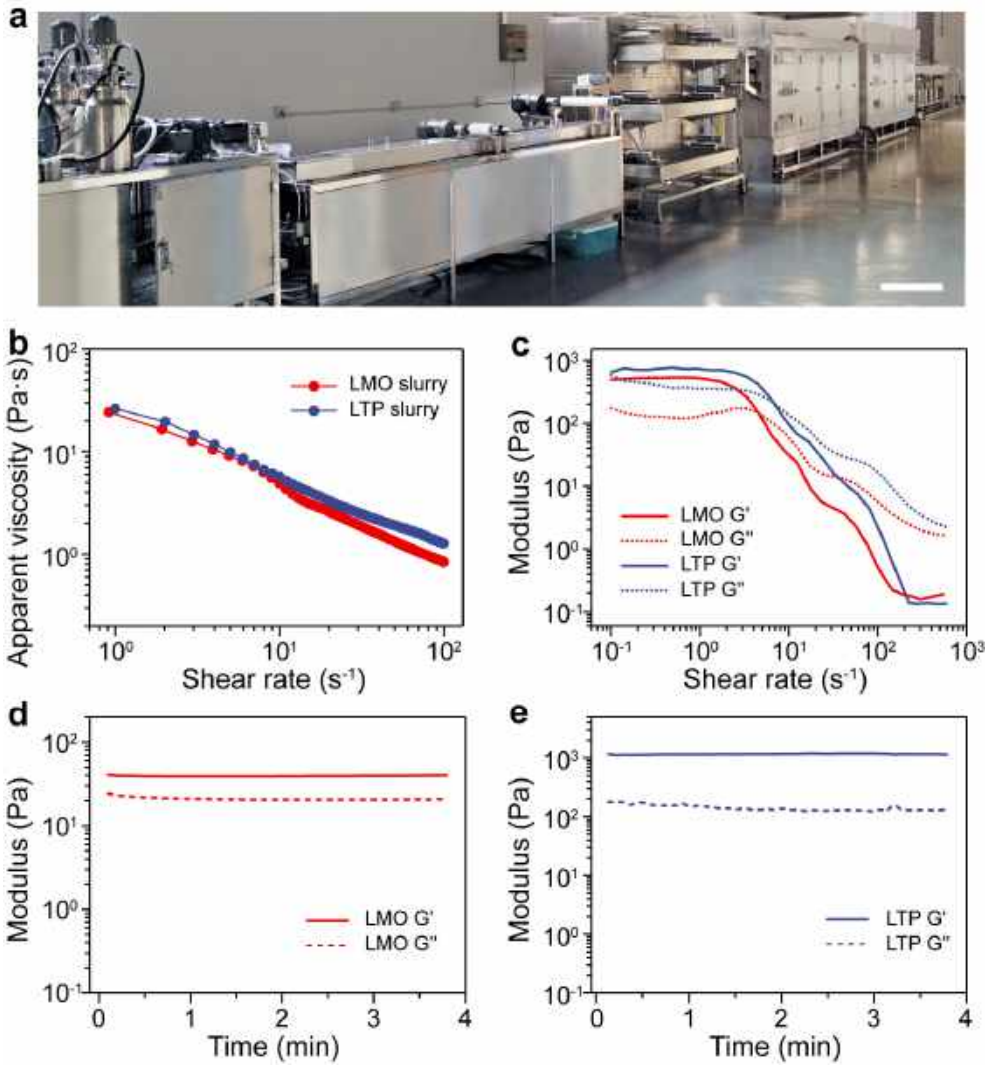

Supplementary Fig. 1 | **a**, Photograph of our continuous production line for extruding fibre batteries. It includes six main processes of slurry mixing, extruding, coagulation, drawing, drying and collecting. Scale bar, 2 m. **b**, Apparent viscosity as a function of shear rate for cathode (LMO) and anode (LTP) inks. **c**, Storage modulus (G′) and loss modulus (G″) as a function of shear rate for cathode and anode inks. **d**, Storage and loss modulus aging as a function of time for cathode ink. **e**, Storage and loss modulus aging as a function of time for anode ink.

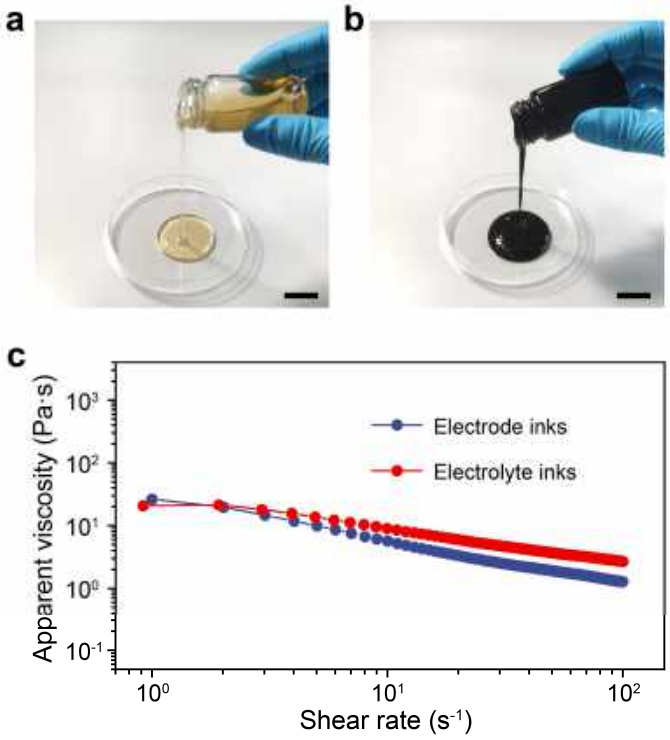

Supplementary Fig. 2 | **a**, **b**, Photographs of the prepared electrolyte and electrode inks for extruded fibre batteries, respectively. **c**, Viscosities of electrode and electrolyte inks at room temperature with respect to the shear rate. The viscosities of electrode and electrolyte inks were designed to match with each other for the prevention of mixing upon extrusion. Scale bars, 2 cm in **a** and **b**.

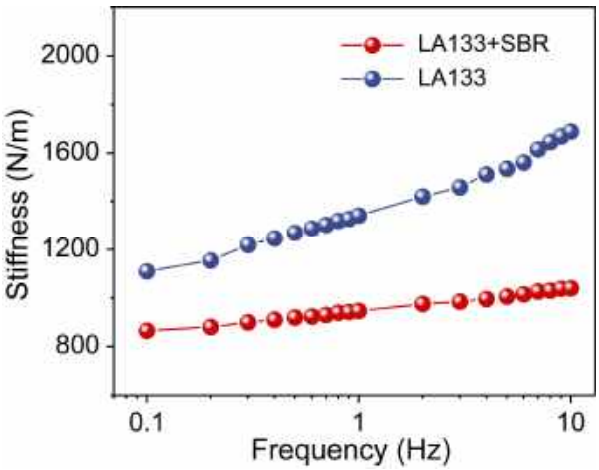

Supplementary Fig. 3 | Graph showing the measured bending stiffness for extruded fibre samples with LA133 + SBR binders and with LA133 binder alone at different frequencies. Samples were 4.2 cm long and ~700 μm in diameter. Bending stiffness was tested at a frequency sweep of 0.1-10 Hz under controlled displacement (50 μm) at 25 °C using a dynamic mechanical analyzer (Q800, TA Instruments).

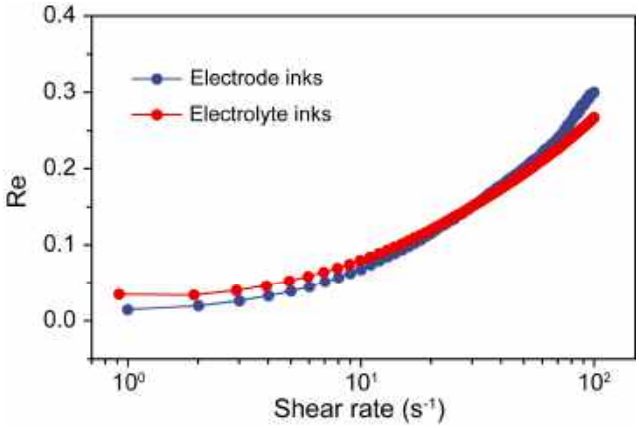

Supplementary Fig. 4 | Reynolds number (Re) as a function of shear rate for electrode inks and electrolyte inks.

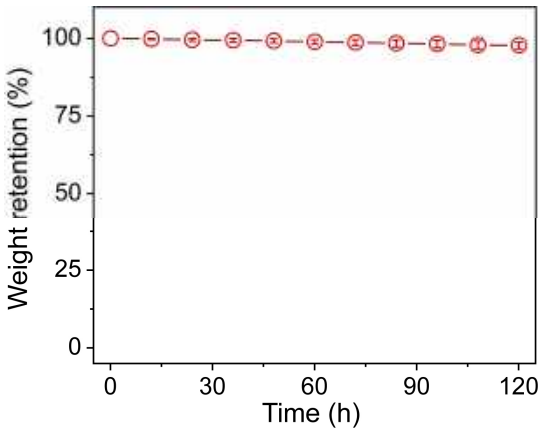

Supplementary Fig. 5 | FLIB encapsulated with flexible PTFE tubes show no change in weight over time, indicating that PTFE can prevent the evaporation of water from the PVA gel electrolyte. Error bars represented the standard deviations of the results from 5 samples.

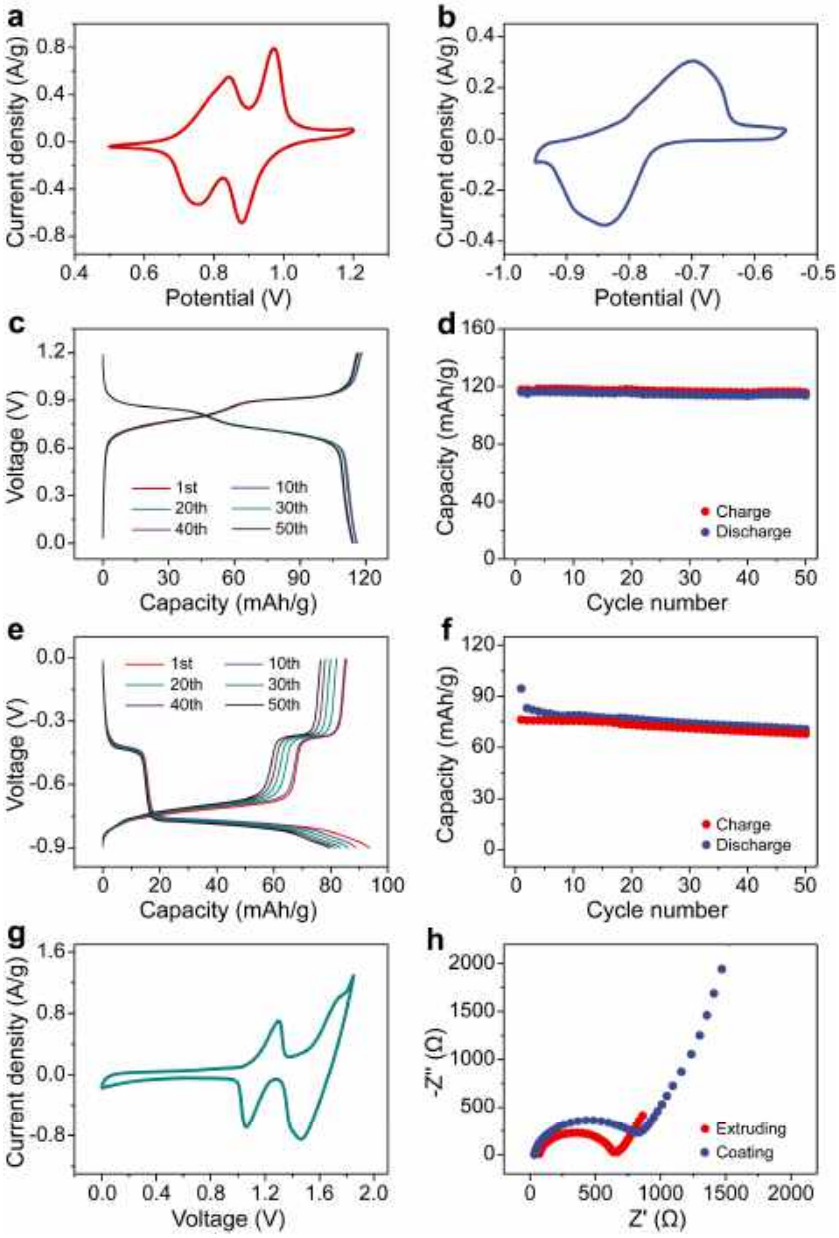

Supplementary Fig. 6 | **a**, Cyclic voltammograms of fibre half-cell with extruded LMO fibre as working electrode, active carbon as counter electrode and Ag/AgCl as reference electrode. **b**, Cyclic voltammograms of fibre half-cell with extruded LTP fibre as working electrode, active carbon as counter electrode and Ag/AgCl as reference electrode. **c**, Charge and discharge profiles of the LMO fibre half-cell. **d**, Cycling stability of the LMO fibre half-cell. **e**, Charge and discharge profiles of the LTP fibre half-cell. **f**, Cycling stability of the LTP fibre half-cell. **g**, Cyclic voltammograms of the full battery with LMO fibre as cathode and LTP fibre as anode. **h**, Electrochemical impedance spectra of fibre batteries fabricated by two different methods. Red curve represented multichannel-extruded fibre batteries. Blue curve corresponded to a fibre battery fabricated through the routine coating process of fibre electrodes.

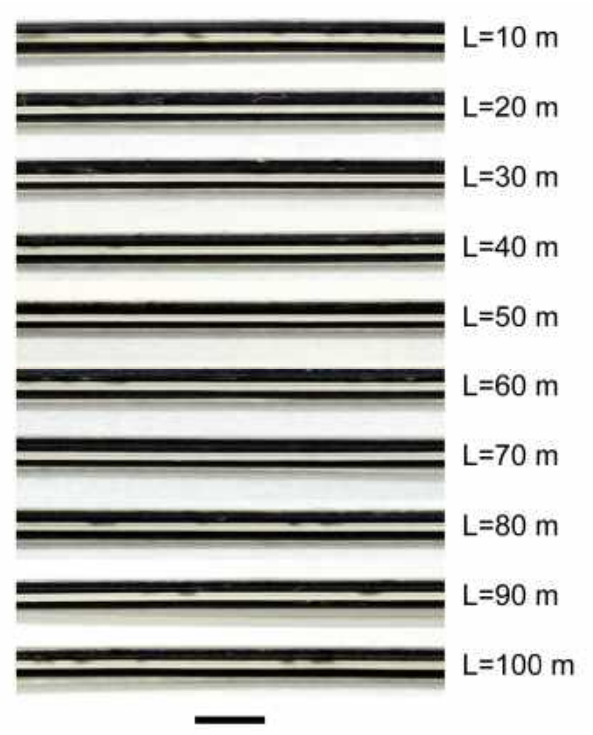

Supplementary Fig. 7 | Optical micrographs of the extruded fibre battery clearly showing the continuous and clear interfaces between two neighboring layers of functional materials across the length of 100 m. Scale bar, 1 mm.

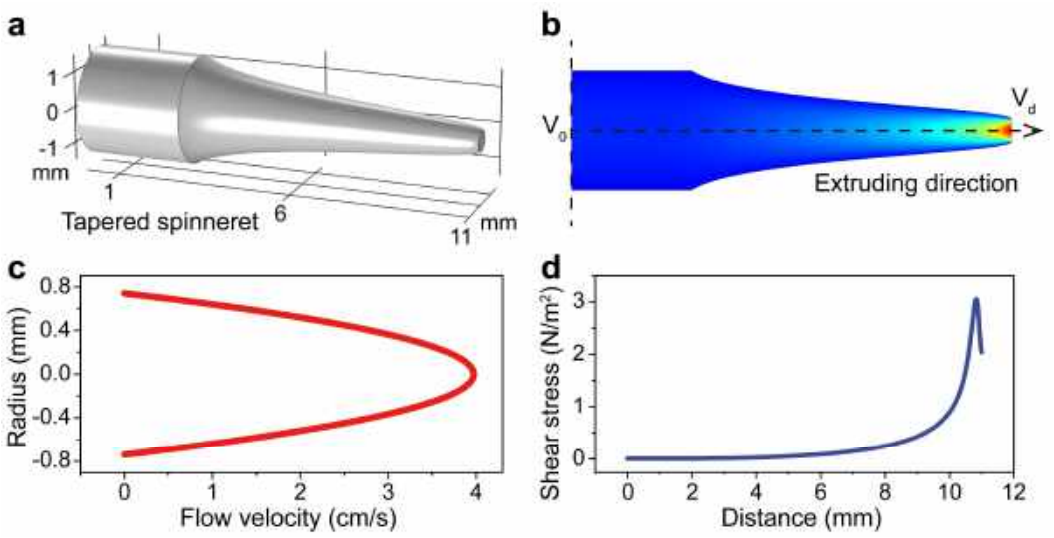

Supplementary Fig. 8 | **a**, **b**, Schematic of the model and side view of the velocity distribution of the tapered channel for the formation of fibre. **c**, Dependence of flow velocity on radius of the tapered channel. **d**, Dependence of shear stress on flowing distance inside the tapered channel.

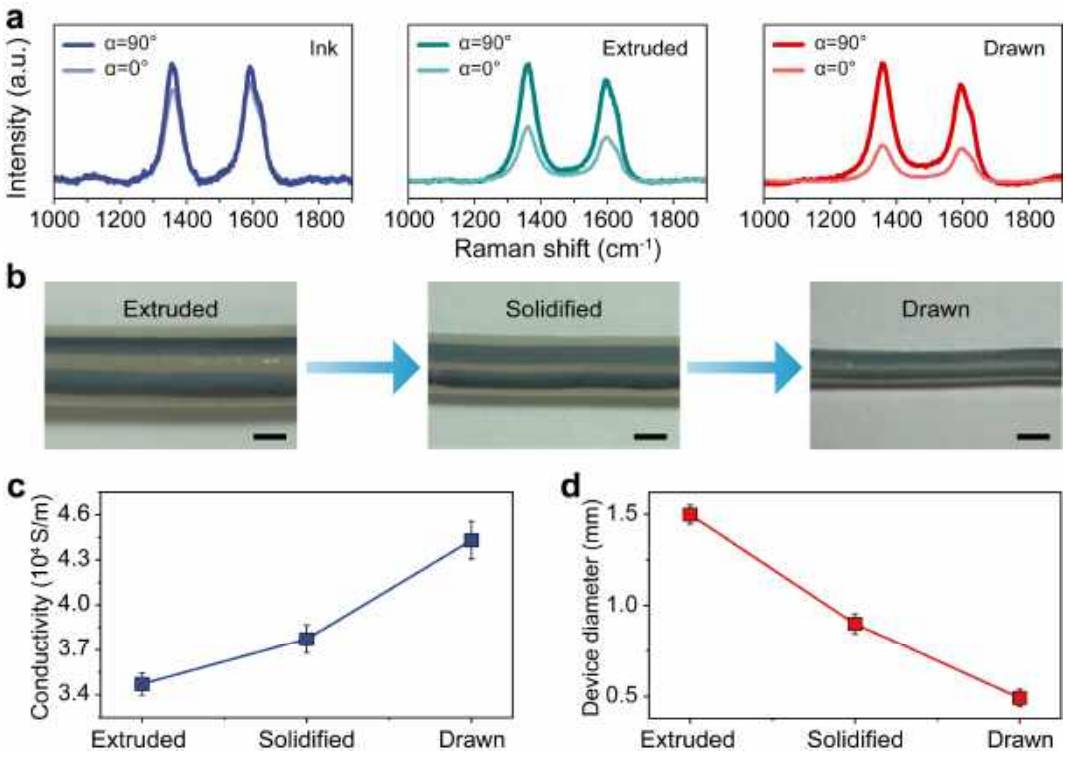

Supplementary Fig. 9 | **a**, Raman spectra showing the degree of orientation of pristine ink, extruded fibre electrode and drawn fibre electrode. **b**, Evolution of device diameters upon extruding, solidifying and drawing. **c**, Electrical conductivities of fibre electrode upon extruding, solidifying and drawing. To highlight the dependence of aligned CNT on conductivities, electrode inks with a CNT mass percent of 90% were used. **d**, Device diameters upon extruding, solidifying and drawing. Error bars represented the standard deviations of the results from five samples. Scale bar, 0.5 mm in **b**.

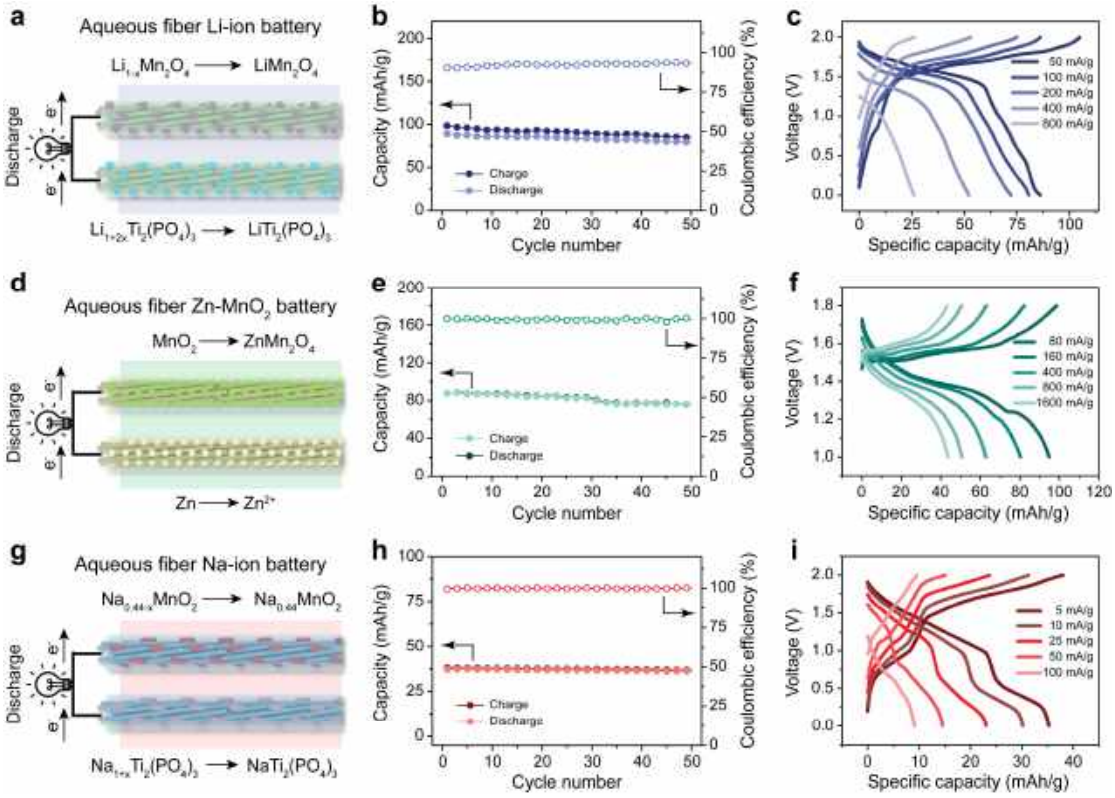

Supplementary Fig. 10 | **a-c**, Schematic illustration, cycling stability and rate performance of aqueous fibre Li-ion batteries (FLIBs), respectively. **d-f**, Schematic illustration, cycling stability and rate performance of aqueous fibre Zn-MnO_2 batteries (FZMBs), respectively. **g-i**, Schematic illustration, cycling stability and rate performance of aqueous fibre Na-ion batteries (FSIBs), respectively.

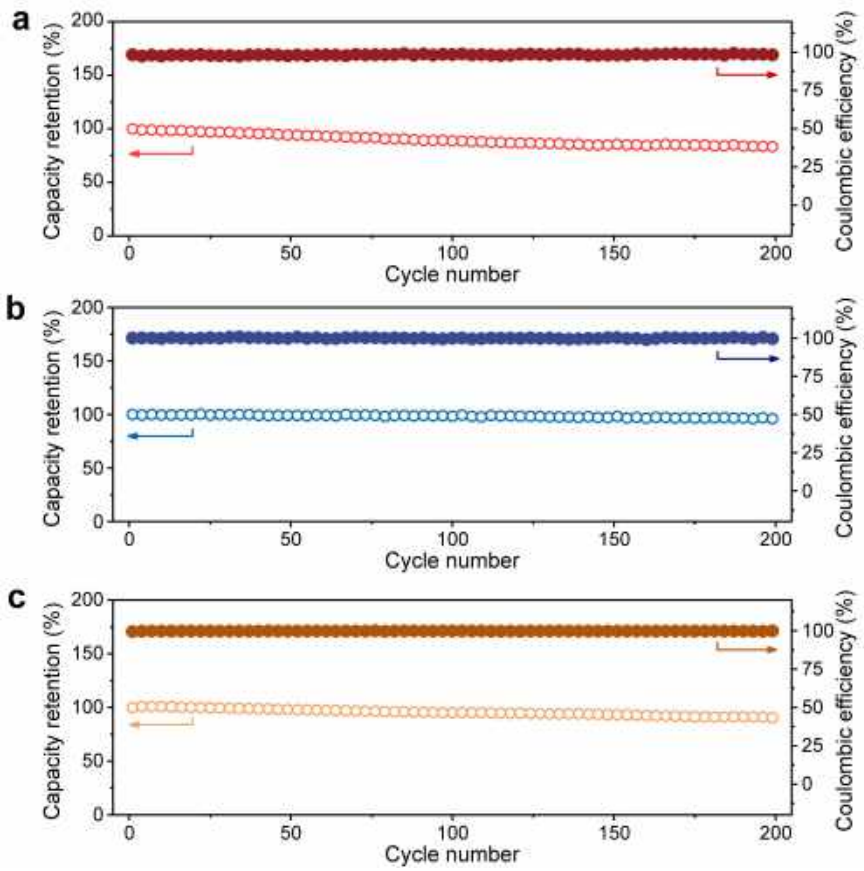

Supplementary Fig. 11 | **a-c**, Cycling stability of aqueous fibre Li-ion batteries (FLIBs) at 5 C rate (**a**), aqueous fibre Zn-MnO_2 batteries (FZMBs) at 6 C rate (**b**), and aqueous fibre Na-ion batteries (FSIBs) at 1 C rate (**c**). All extruded fibres displayed capacity retention of > 80% over 200 cycles, making them suitable for practical applications.

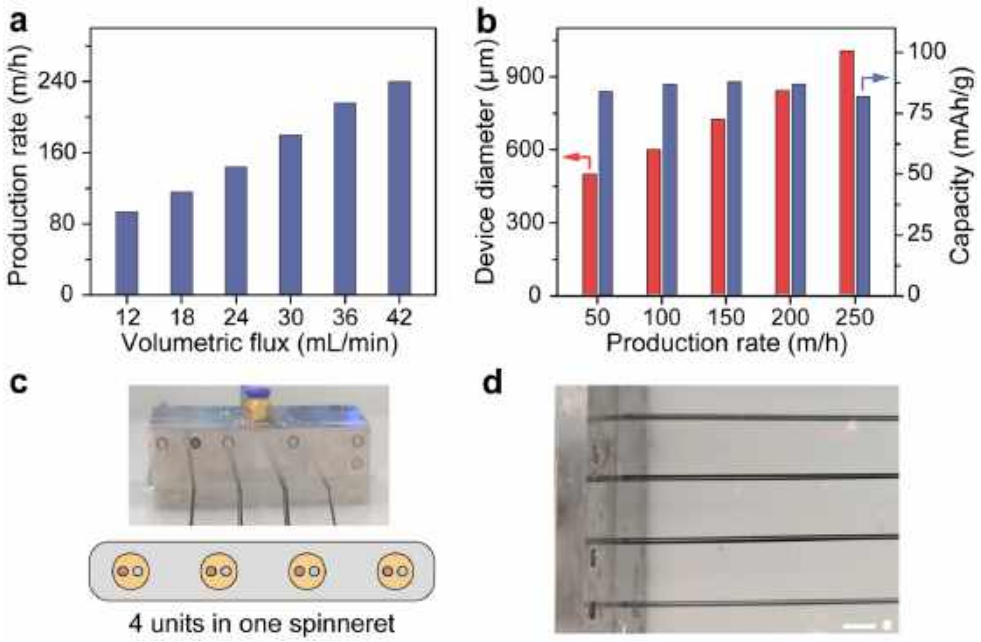

Supplementary Fig. 12 | **a**, Dependence of production rate on volumetric flux of functional inks. **b**, Dependence of device diameter and specific capacity on production rate. **c**, Photograph and schematic illustration of the spinneret with 4 extruding units. **d**, Photograph of the continuous production of 4 fibre batteries from a 4-extruding-unit spinneret. Scale bar, 1 cm in **d**.

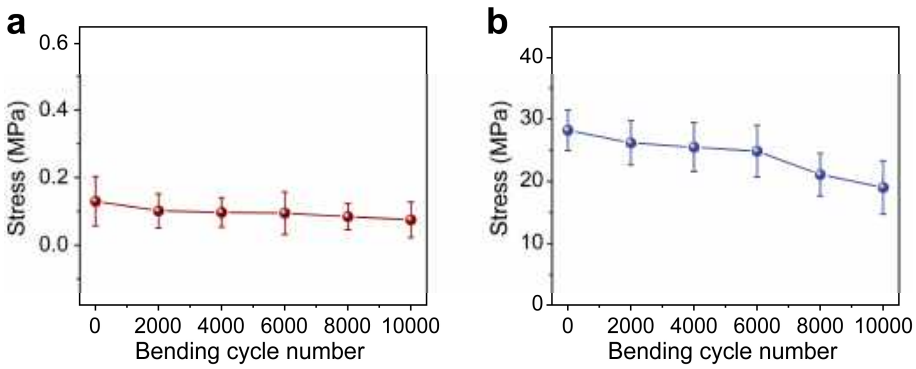

Supplementary Fig. 13 | **a**, **b**, Maximal stress at various bending cycles for fibre batteries fabricated by solution-extrusion (**a**) and sequential coating (**b**). Fibre batteries produced using solution-extrusion are more flexible than those made by sequential coating. Lower internal stress indicates higher flexibility. Error bars are standard deviations (n = 5 samples per test).

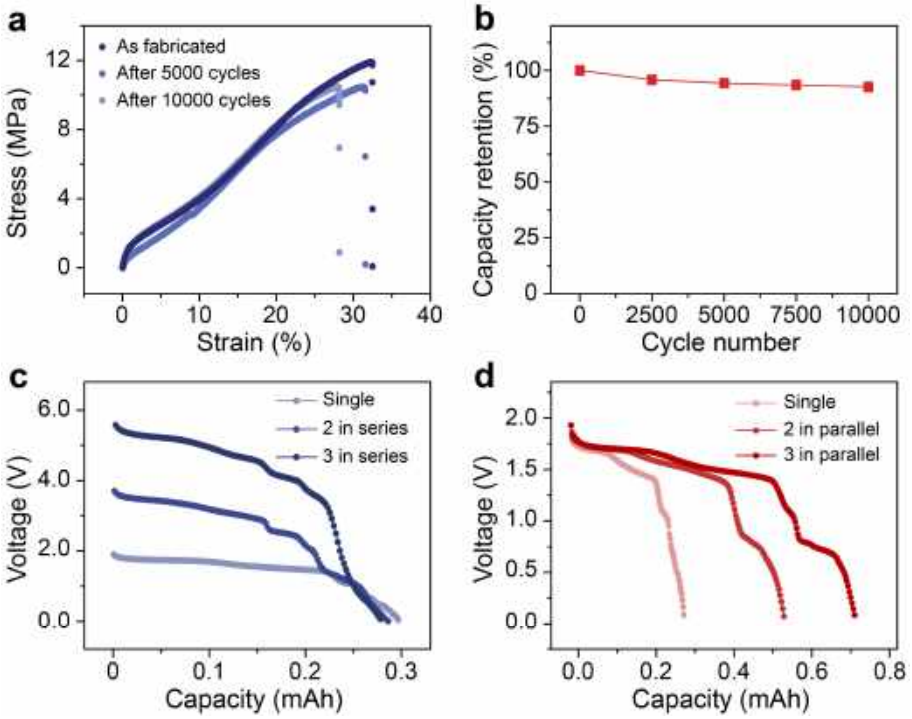

Supplementary Fig. 14 | **a**, Stress-strain curves of FLIBs before and after bending for 5000 and 10000 cycles. **b**, Dependence of capacity retention on bending cycle number of FLIBs. **c**, Discharge profiles for one, two and three FLIB(s) in series. **d**, Discharge profiles for one, two and three FLIB(s) in parallel.

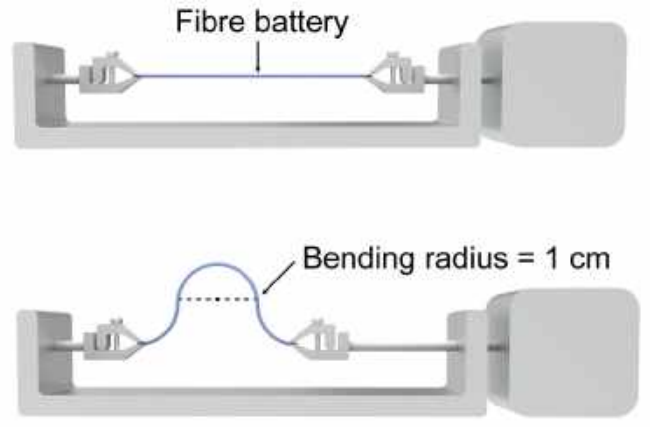

Supplementary Fig. 15 | Schematic of a deformation test performed on a set of home-made stepper motors. The extruded fibre battery is dynamically bent to a bending radius of ~1 cm at a frequency of 2.5 Hz using a 0.1 N load.

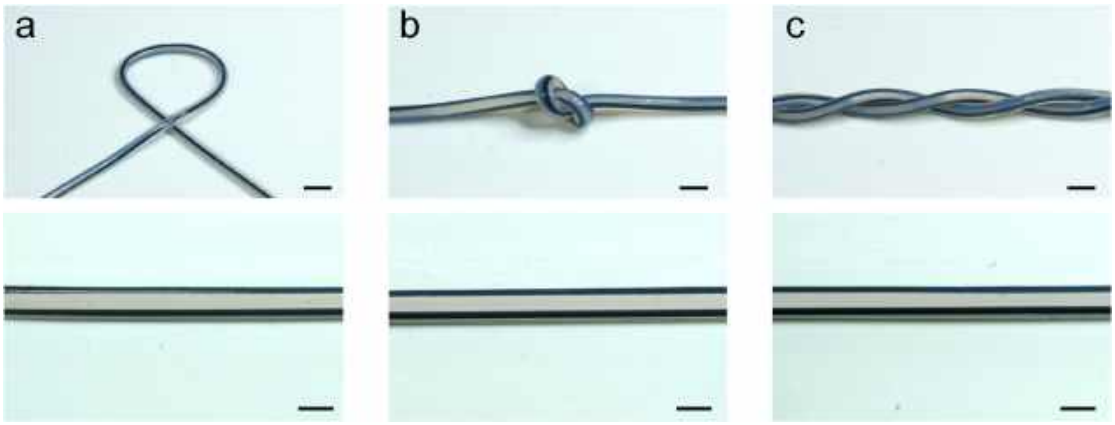

Supplementary Fig. 16 | **a-c**, Optical micrographs of an extruded fibre battery after 10,000 cycles of bending (**a**), knotting (**b**) and twisting (**c**) show the interfaces between the functional materials remained stable. Scale bars, 500 μm.

Supplementary Fig. 17 | Photograph of extruded fibre batteries with increasing diameters. Scale bar, 500 μm.

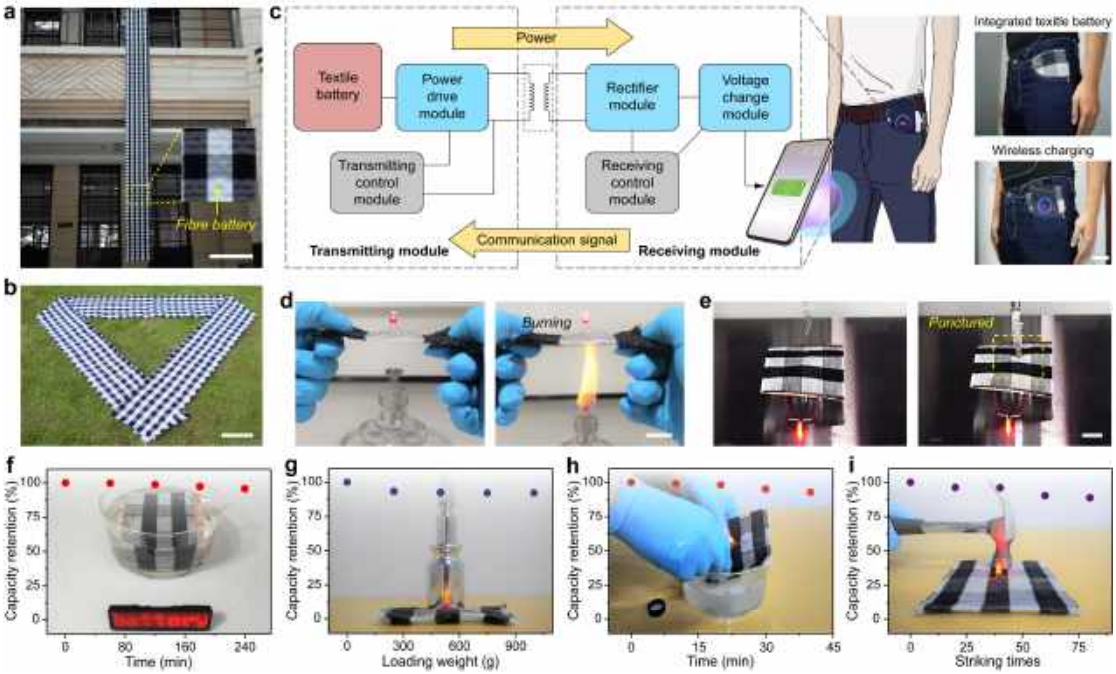

Supplementary Fig. 18 | **a**, **b**, Flexible FLIB textile with length over 10 m at spread and folded states, respectively. **c**, Schematic illustration, controlling circuit and corresponding photographs of the FLIB textile powering a mobile phone *via* wireless charging. **d**, Photographs show an FLIB textile placed over a burning alcohol lamp continued to function. No flames or explosions were seen because the aqueous gel electrolyte used is non-flammable. **e**, FLIB textile against the puncture by a blade. **f-i**, FLIB textile stably working upon varying usage scenarios including in water, under pressing, under washing and under striking. Scale bars, 1 m in **a**, 0.5 m in **b**, 5 cm in **c**, 2 cm in **d** and **e**.

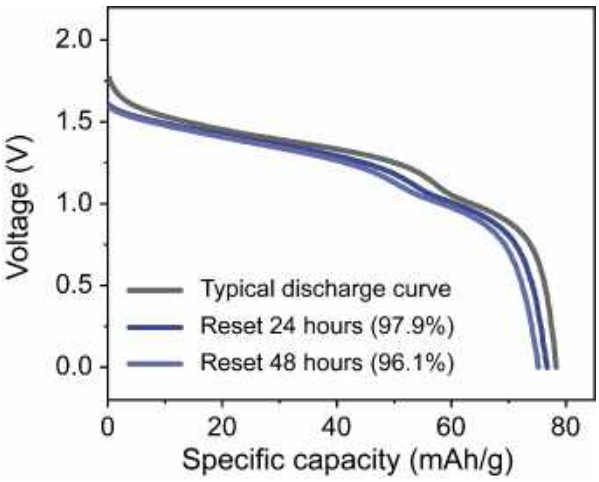

Supplementary Fig. 19 | Self-discharging behavior of the FLIB. The discharge curves were traced after resting at open-circuit voltage.

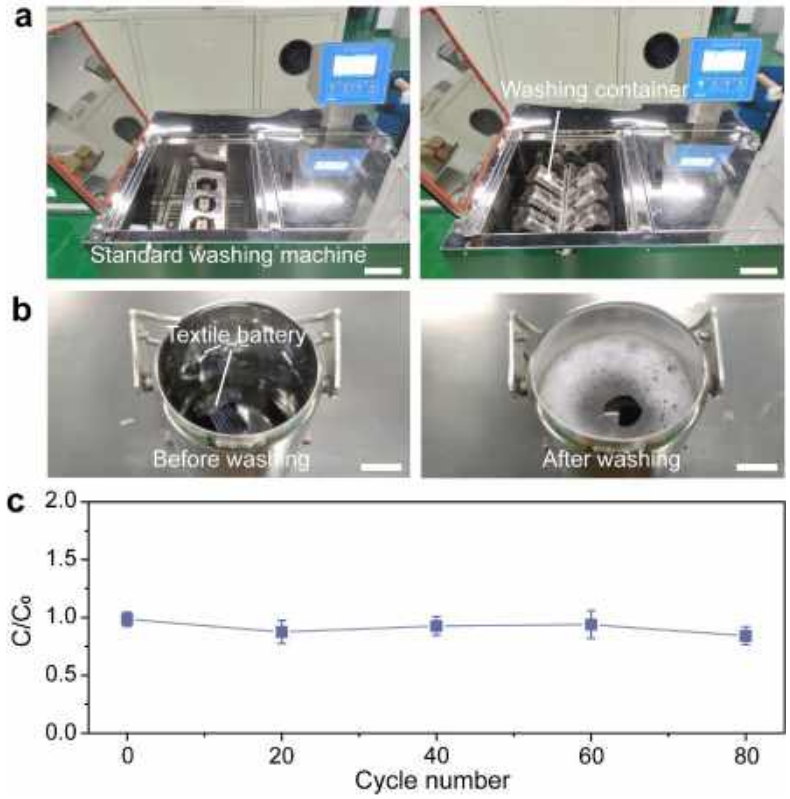

Supplementary Fig. 20 | **a**, Photographs of the standard washing machine used in the washing test for textile batteries woven from FLIBs. **b**, Photographs of the washing test. **c**, Capacity retention of the textile battery did not change after 80 washing cycles. Scale bars, 10 cm in **a**, 2 cm in **b**. Error bars in **c** are standard deviations (n = 5 samples per wash cycle).

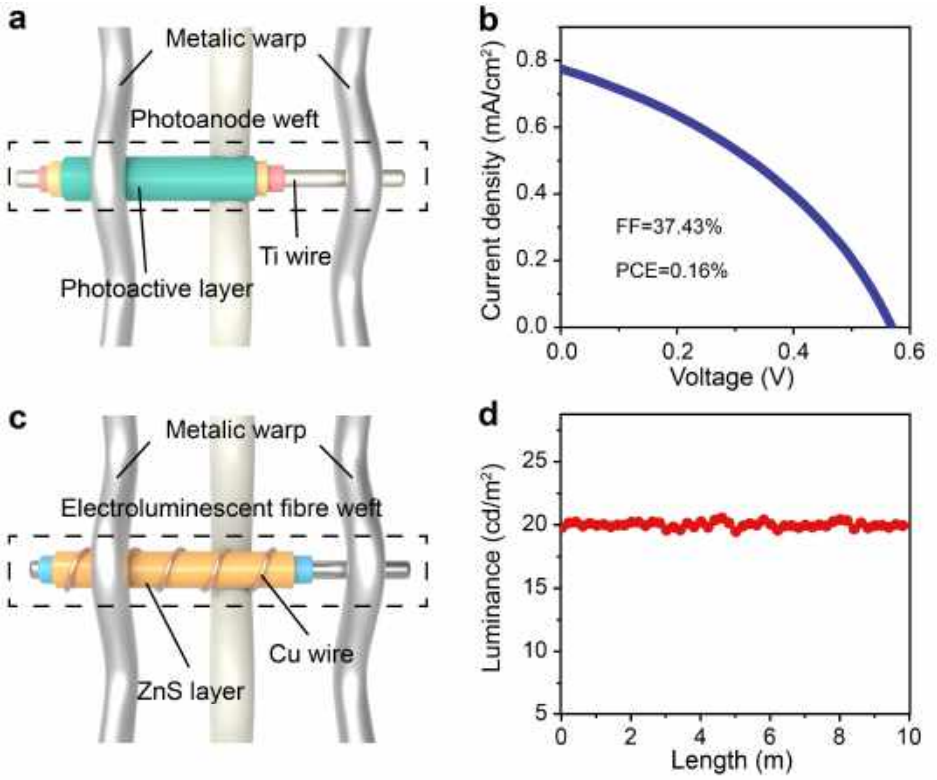

Supplementary Fig. 21 | **a**, Schematic of a woven energy harvesting module. **b**, Current density-voltage characteristics of the energy harvesting module, exhibiting a short-circuit current density of 0.78 mA/cm^2 and an open-circuit voltage of 0.56 V. **c**, Schematic of a woven light luminescent module. **d**, Luminance-length characteristic of the luminescent fibre.

Supplementary Table 1 | Materials used to produce solution-extruded fibre batteries.

Material	Standard	Manufacturer
LA133 binder	15 wt%	Chengdu Yindile Energy Technology Co., Ltd.
CNT aqueous dispersion	TNWPM-15-M8	Chengdu Organic Chemicals Co., Ltd.
LMO	99.9%	Sinopoly New Energy Investment Co., Ltd.
SBR	GF576	OMNOVA Solutions
LTP	99.9%	Jiangxi Kingli Science Share Co., Ltd.
PVA	1799	Aladdin
Chitosan	degree of deacetylation > 80%	Golden-Shell Pharmaceutical Co., Ltd.
Li_2SO_4	Analytical reagent	Aladdin
Acetic acid	Analytical reagent	Sinopharm
NaOH	Analytical reagent	Sinopharm
MnO_2	99 wt%	Adamas
Zn powder	99.99 wt%	Aladdin

Supplementary Table 2 | Comparison of active materials, assembly process, specific capacity and production length of fibre Li-ion batteries.

Ref.	Cathode/Anode	Assembly	Electrolyte	Specific capacity	Length
6	$LiMn_2O_4$–CNT Polyimide–CNT	Multiple steps	Aqueous	0.0012 mAh/cm at 600 C	0.2 m
7	$LiMn_2O_4$–CNT $Li_4Ti_5O_{12}$–CNT	Multiple steps	Organic	0.0028 mAh/cm at 0.01 mA	0.1 m
8	$LiMn_2O_4$–CNT $Li_4Ti_5O_{12}$–CNT	Multiple steps	Organic	0.0036 mAh/cm at 0.02 mA/cm	0.1 m
9	$LiMn_2O_4$–carbon cloth TiO_2–rGO	Multiple steps	Organic	0.015 mAh/cm at 0.0170 mA	0.3 m
10	$LiFePO_4$–carbon fibre $Li_4Ti_5O_{12}$–carbon black	Multiple steps	Solid-state	0.0215 μAh/cm at 26 μA/cm^2	0.3 m
11	$LiMn_2O_4$-CNT Si–CNT	Multiple steps	Organic	0.022 mAh/cm at 0.2 C	0.1 m
This work	$LiMn_2O_4$–CNT $LiTi_2(PO_4)_3$–CNT	One step	Aqueous	0.05 mAh/cm at 50 mA/g	Kilometres

Caption for Supplementary Movie

Supplementary Movie 1 | Continuous production of fibre batteries

Supplementary Movie 2 | FLIB textile charges a phone

Supplementary Movie 3 | FLIB textile charges a phone under folding

Supplementary Movie 4 | FLIB textile charges a phone when heated by a flame

Supplementary Movie 5 | FLIB textile charges a phone when punctured by a blade

Supplementary Movie 6 | FLIB textile charges a phone after washing

Supplementary Movie 7 | FLIB textile charges a phone when rolled by a motorbike

Supplementary Movie 8 | Weaving the textile display for the smart tent system

Supplementary References

1. Mo, F. et al. An overview of fiber-shaped batteries with a focus on multifunctionality, scalability, and technical difficulties. *Adv. Mater.* **32**, 1902151 (2020).
2. Zhu, Y. et al. Flexible 1D batteries: recent progress and prospects. *Adv. Mater*. **32**, 1901961 (2020).
3. Huang, Q. et al. Textile-based electrochemical energy storage devices. *Adv. Energy Mater*. **6**, 1600783 (2016).
4. Gao, Z. et al. Flexible self-powered textile formed by bridging photoactive and electrochemically active fibre electrodes. *J. Mater. Chem. A* **7**, 1447–1454 (2019).
5. Zhang, J. et al. Flexible and stretchable mechanoluminescent fibre and fabric. *J. Mater. Chem. C* **5**, 8027–8032 (2017).
6. Zhang, Y. et al. A fibre-shaped aqueous lithium ion battery with high power density. *J. Mater. Chem. A* **4**, 9002–9008 (2016).
7. Ren, J. et al. Elastic and wearable wire-shaped lithium-ion battery with high electrochemical performance. *Angew. Chem. Int. Ed.* **53**,7864-7869 (2014).
8. Zhang, Y. et al. Super-stretchy lithium-ion battery based on carbon nanotube fibre. *J. Mater. Chem. A* **2**, 11054–11059 (2014).
9. Hoshide, T. et al. Flexible lithium-ion fibre battery by the regular stacking of two-dimensional titanium oxide nanosheets hybridized with reduced graphene oxide. *Nano Lett.* **17**, 3543–3549 (2017).

10. Yadav, A., De, B., Singh, S. K., Sinha, P. & Kar, K. K. Facile development strategy of a single carbon-fibre-based all-solid-state flexible lithium-ion battery for wearable electronics. *ACS Appl. Mater. Interfaces* **11**, 7974–7980 (2019).
11. Weng, W. et al. Winding aligned carbon nanotube composite yarns into coaxial fibre full batteries with high performances. *Nano Lett.* **14**, 3432–3438 (2014).